

Abstract

We carried out a statistical study of equatorial dipolarization fronts (DFs) detected by the Magnetospheric Multiscale mission (MMS) during the full 2017 Earth’s magnetotail season. We found that two DF classes are distinguished: class I (74.4%) corresponds to the standard DF properties and energy dissipation and a new class II (25.6%). This new class includes the six DF discussed in Alqeeq et al. (2022) and corresponds to a bump of the magnetic field associated with a minimum in the ion and electron pressures and a reversal of the energy conversion process. The possible origin of this second class is discussed. Both DF classes show that the energy conversion process in the spacecraft frame is driven by the diamagnetic current dominated by the ion pressure gradient. In the fluid frame, it is driven by the electron pressure gradient. In addition, we have shown that the energy conversion processes are not homogeneous at the electron scale mostly due to the variations of the electric fields for both DF classes.

1 Introduction

Magnetotail earthward fast plasma flows (Baumjohann et al., 1990) or bursty bulk flows (BBF, Angelopoulos et al., 1992) play a major role in the energy, plasma and magnetic flux transport from the magnetotail to the inner magnetosphere (e. g., Angelopoulos et al., 1994). They are often, although not always (Richard et al., 2022), accompanied by a sharp and transient increase of the northward component of the magnetic field called dipolarization fronts (DFs). DFs are considered as tangential discontinuities (velocity and magnetic field variations are tangential to the front so with no normal component of the magnetic field and no plasma flux flowing through it) separating a relatively cold dense plasma at rest from a hot tenuous plasma in rapid motion (e. g., Sergeev et al., 2009; H. S. Fu, Khotyaintsev, Vaivads, André, & Huang, 2012). The origin of the fast flows and their related DFs is still a matter of debate. The main formation mechanisms currently studied are magnetic reconnection (e. g., Sitnov et al., 2009; Drake et al., 2014), kinetic ballooning interchange instability (e. g., Pritchett & Coroniti, 2010; Panov et al., 2022) and low entropy magnetic flux tubes (e. g., Pontius & Wolf, 1990; Wolf et al., 2009). Fast plasma flows and DFs can be related to a global scale substorm activity or appear as isolated structures. Regarding the spatial scale of DFs, R. Nakamura et al. (2004) investigated spatial gradients of high-speed flows in the mid-tail plasma sheet using multi-satellite Cluster observations (Escoubet et al., 2001). They found that the typical scales of fast flows/BBFs are about 2–3 R_E in the dawn-dusk direction and 1.5–2 R_E in the north-south direction. Using THEMIS data (Angelopoulos, 2008), J. Liu et al. (2013) also estimated the dawn-dusk size of dipolarizing flux bundles (localized areas of dipolarized flux tubes) between 1 and 3 R_E . These scales can be considered as upper limits for DFs which correspond to the flow front or can be embedded in these fast flows. Along the direction of propagation, the DF thickness was shown to be about a few ion inertial lengths (e. g., Runov et al., 2009; Schmid et al., 2011). Runov et al. (2011a) summarized the general characteristics of DFs as an asymmetric bipolar variation of the northward component of the magnetic field associated with ion density and pressure decrease and ion temperature increase after the DF passage. However, DFs can be represented in different categories. Schmid et al. (2015) discussed four categories of DFs. They performed a statistical study of the temperature and density variations during DF crossings, using 9 years (2001–2009) of Cluster data. They found $\sim 54\%$ of DFs belonging to the category A defined by a temperature increase while the density and the thermal pressure decrease across the DF. The second most important category B (28%) corresponds to an increase of the density while the temperature decreases and the thermal pressure shows no significant change; it is also associated with slower plasma flow and larger background northward magnetic field component than category A. Based on these results, the authors suggested that fast flows could be generated by reconnection in the magnetotail producing DFs of category A. Then the latter could evolve into a DF of category B during their earthward propagation toward the braking region. Following this

83 first study, Schmid et al. (2019) identified two DF subcategories depending on the sign
 84 of the magnetic field dip preceding the DF. A positive dip was found to be correlated
 85 with the enhancement of the perpendicular and diamagnetic currents flowing ahead of
 86 the DF. A negative dip was more correlated with field-aligned currents and was suggested
 87 to be related to flux ropes and/or resulting of localized guide field reconnection.

88 DFs host different mechanisms of particle acceleration (see H. Fu et al., 2020, for
 89 a review) and are thought to play an important role in the magnetosphere global energy
 90 cycle. Due to the enhancement of the cross-tail current at DF and the motional electric
 91 field, energy is dissipated along their earthward propagation. Depending on assumed DF
 92 sizes in the azimuthal and vertical directions a significant energy dissipation occurs (e.
 93 g., Angelopoulos et al., 2013). Various statistical studies have been performed about the
 94 energy conversion rate $\mathbf{J} \cdot \mathbf{E}$ associated with DFs (where \mathbf{J} is the current density and
 95 \mathbf{E} the electric field). Using Cluster data, Hamrin et al. (2014) found that fast flows with
 96 a velocity peak behind the front (equivalent to a growing Flux Pileup Region FPR as
 97 introduced by H. S. Fu, Khotyaintsev, Vaivads, André, Sergeev, et al. (2012)) were de-
 98 celerated and energy was radiated, i.e., converted from particles to fields. For fast flows
 99 with velocity peak detected ahead or at DF (decaying FPR as introduced by H. S. Fu,
 100 Khotyaintsev, Vaivads, André, Sergeev, et al. (2012)), no braking signature was detected
 101 and energy was dissipated i. e., transferred from fields to particles. Also from Cluster
 102 statistical data analysis, Huang et al. (2015) found that the energy was significantly dis-
 103 sipated at DFs. More recently and using the high temporal and spatial resolutions of MMS
 104 data (Burch et al., 2016), Zhong et al. (2019) analysed 122 DFs gathered from May to
 105 August 2017 and found that the electromagnetic energy is mostly transferred to plasma
 106 at DF ($\mathbf{J} \cdot \mathbf{E} > 0$). In the fluid frame, they found that $\mathbf{J} \cdot \mathbf{E}' = \mathbf{J} \cdot (\mathbf{E} + \mathbf{v}_e \times \mathbf{B})$ could be
 107 positive and negative but on average it is very small. Khotyaintsev et al. (2017) com-
 108 pared Cluster observations with results from 3D Particle-In-Cell (PIC) simulations. They
 109 concluded that the energy dissipation in the satellite frame was mainly due to the mo-
 110 tional electric field and the ion contribution to the cross-tail current density. No signif-
 111 icant energy conversion was found in the DF frame (defined by using the ion velocity at
 112 the DF). Partitioning of the energy at DFs between ions and electrons was investigated
 113 by Sitnov et al. (2018) using kinetic energy dissipation parameter introduced by Y. Yang
 114 et al. (2017). Ions were heated at and ahead of DFs, whereas electrons were heated at
 115 and behind due to the long-wavelength Lower-Hybrid Drift instability (LHDI). There-
 116 fore, it was suggested that both contributions lead to an important energy dissipation.
 117 However, such an analysis applied to in-situ MMS data did not provide clear signatures
 118 (Zhong et al., 2019). Still from 3D PIC simulations, T. K. M. Nakamura et al. (2019)
 119 reported energy dissipation within the density gradient layer at DF (in the fluid frame)
 120 due to the LHDI.

121 Alqeeq et al. (2022) investigated in detail six DF events observed by MMS in the
 122 Earth's magnetotail on July 23, 2017. The energy conversion processes were also anal-
 123 ysed based on the calculation of the $\mathbf{J} \cdot \mathbf{E}$ term. They found that, in the frame of the
 124 satellite, the energy is dissipated (dissipation or load region) ahead of the DF but trans-
 125 ferred from the plasma to the fields behind the front (dynamo or generator region). This
 126 inversion is caused by the inversion of the current density as the motional electric field
 127 does not change sign during the DF crossing. In the fluid frame, the energy was found
 128 to be transferred from the plasma to the fields as also found in a previous MMS single
 129 DF event (Z. H. Yao et al., 2017). This dynamo region could contribute to the slowdown
 130 of the fast flow. Then, by calculating the standard deviation (SD) of the current den-
 131 sity and the electric field measurements from the four satellites, they found that this en-
 132 ergy conversion is not homogeneous at the electron scale due to the electric variations
 133 produced by the electron pressure gradient. The Lower-Hybrid Drift (LHD) waves have
 134 been suggested as a possible source of these electric field variations although due to the
 135 time averaging of all data (0.3 s), the high-frequency part of the spectra was filtered out.
 136 These waves are expected to be generated by the large density gradient at DFs (e. g.,

137 Sergeev et al., 2009; Divin, Khotyaintsev, Vaivads, & André, 2015; Le Contel et al., 2017;
 138 J. Yang et al., 2017; C. M. Liu et al., 2018; Hosner et al., 2022) generating ripples on the
 139 front at the electron scales and thus leading to the non homogeneity of the energy con-
 140 version process (Pan et al., 2018).

141 In order to extend these case study results, we have carried out a statistical study
 142 of the energy conversion processes at DFs using MMS observations from the full 2017
 143 magnetotail season. Based on this statistical investigation, we show that two subclasses
 144 of DF can be distinguished depending on the magnetic field profile and sign of the en-
 145 ergy conversion term. These two subclasses, although sharing some common properties
 146 with Schmid et al. (2019) subcategories, are not identical. We also confirm the non-homogeneity
 147 of the energy conversion processes at electron scales. The present study is organized as
 148 follows: data, methods and event selection are described in section 2, and an overview
 149 of the statistical DF properties is presented in section 3. In section 4, we present cross-
 150 validation of current density calculations, ion and electron dynamics are investigated thanks
 151 to the Ohm’s law in section 5, then the energy conversion processes in the vicinity of DFs
 152 are scrutinized in section 6. The global results of this statistical study are summarized
 153 and discussed in section 7. Finally, we conclude in section 8.

154 2 Data, Methods and Event Selection

155 2.1 Data and Selection criteria

156 Data used for this statistical study are provided by the following MMS instruments:
 157 the Fluxgate Magnetometer (FGM) in burst mode (Russell et al., 2016), the Electric Dou-
 158 ble Probe (EDP) in fast survey mode (Ergun et al., 2016; Lindqvist et al., 2016), the Fast
 159 Plasma Instrument (FPI) (Pollock et al., 2016), and the Hot Plasma Composition An-
 160 alyzer (HPCA) (Young et al., 2016).

161 We have selected DFs using burst FGM and FPI (DIS and DES) nominal L2 data
 162 in *GSE* from the full magnetotail season of 2017 (end of April to end of August). In or-
 163 der to automatically identify DF signature, we have used an Artificial Intelligence Data
 164 Analysis (AIDApY) routine (Lapenta & AIDA H2020 Team, 2019) based on the differ-
 165 ence between maximum and minimum values of physical quantities (n , V_i , B , ...) com-
 166 puted within a 60 s sliding window. A typical DF signature is defined by the following:

- 167 • an increase of the northward B_z component of the magnetic field > 6 nT,
- 168 • an increase of the X component of the ion velocity > 150 km/s,
- 169 • an increase of both parallel and perpendicular temperatures of ions (> 5 keV) and
 170 electrons (> 1 keV),
- 171 • a decrease of both ion and electron densities (only corresponding to a negative value
 172 of the difference between maximum and minimum values without specific thresh-
 173 old value).

174 This first automatic selection step provided 857 DF events. The following constraints
 175 are checked manually:

- 176 • Electron partial moment data have to be available at least 60 s before and 60 s
 177 after DF crossing. DF crossing time t_0 is defined by the maximum of B_z in the
 178 selected time interval.
- 179 • Only DFs near the Earth’s magnetotail equator are kept using the following con-
 180 straint $|B_x| < 5$ nT.

181 Indeed, electron partial moment data computed by the FPI team are necessary due to
 182 the very low density values (and low counts) in the magnetotail (see Alqeeq et al., 2022,
 183 for more details). Due to these constraints, the new DF list is reduced to 132 DF events.

184 These criteria are quite similar to those used in previous DF statistical studies (e. g.,
 185 Zhong et al., 2019; Li et al., 2015; J. Liu et al., 2013). For instance, Zhong et al. (2019)
 186 limited their DF selection by considering only plasma densities between 0.2 to 0.9 p.cm⁻³
 187 and burst mode data available at least 15 s before and 30 s after the DF. On the other
 188 hand, J. Liu et al. (2013) considered just the measurements in the magnetotail region
 189 defined by $-30 R_E < X_{GSM} < -6 R_E$ whereas Li et al. (2015) investigated the region
 190 defined by $X_{GSM} \leq -8 R_E$ and $|Y_{GSM}| \leq 10 R_E$.

191 In the present study, the selection criteria are applied to each spacecraft and only
 192 events observed by all four MMS satellites are kept. Finally, all selected DF events have
 193 been individually validated by a visual check.

194 Figures 1A and B, show that all selected DFs are located in the region satisfying
 195 $-25 \leq X_{GSE} \leq -10 R_E$ and $|Y_{GSE}| \leq 15 R_E$. The DF distribution is quite symmet-
 196 ric in the equatorial plane while it is shifted toward the north mostly due to the seasonal
 197 effect (inclination of the rotation axis of the Earth's toward the Sun during the North
 198 hemisphere summer) (see Figure 2A and B). The external limit at $X_{GSE} \sim -25 R_E$ cor-
 199 responds to the MMS apogee in 2017. The internal limit at $X_{GSE} \sim -10 R_E$ is a bit
 200 farther from the Earth than the beginning of the fast survey mode associated with the
 201 ROI ($X_{GSE} < 9 R_E$). Therefore the outer and inner limits are related to the MMS apogee
 202 and ROI and do not mean that DF cannot be detected nearer or farther from the Earth.

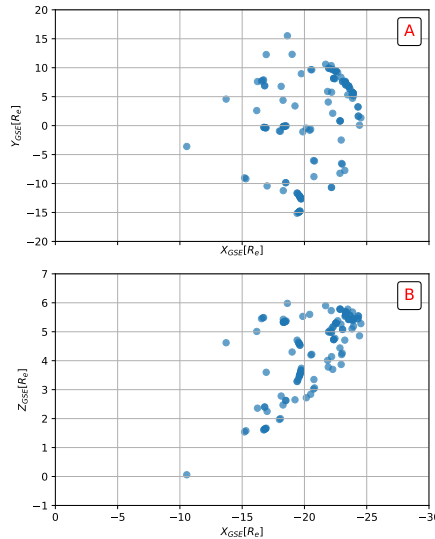


Figure 1. An overview of all DFs events that match the selection criteria. Panels (A) XY and (B) XZ position of MMS during the observations of the 132 DF events in GSE .

203 2.2 Methods

204 DFs are characterized as a sharp increase of the northward component of the mag-
 205 netic field B_z which are generally preceded by a short decrease, a dip (e. g., Runov et
 206 al., 2009; Sergeev et al., 2009; Huang et al., 2015; Schmid et al., 2015; Zhong et al., 2019).
 207 DF signatures are usually displayed in a local coordinate system obtained from a Min-
 208 imum Variance Analysis (Sonnerup & Scheible, 1998) applied on magnetic fields data
 209 MVAB of a single spacecraft (e. g., Huang et al., 2015; C. M. Liu et al., 2018) and/or
 210 from a timing analysis (TA) in case of multi-spacecraft missions (e. g., H. S. Fu, Khotyaint-
 211 sev, Vaivads, André, Sergeev, et al., 2012).

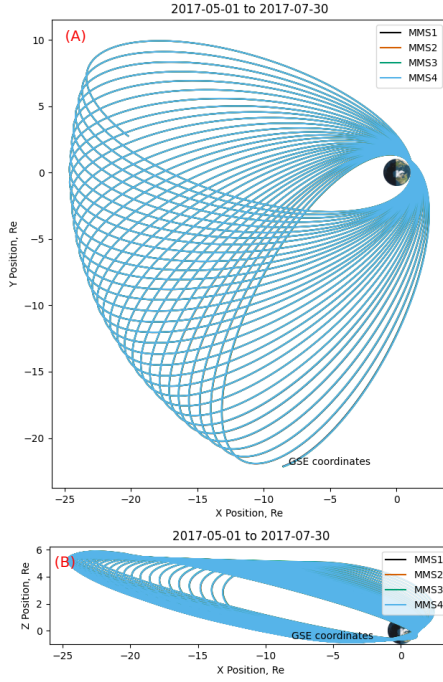


Figure 2. MMS orbit for the magnetotail season from 2017 (1st of May to end of July in *GSE* frame. Panel (A) shows MMS orbit in *XY* plane and (B) in *XZ* plane.

212 In the present study, MVAB is applied on the four spacecraft average of the mag-
 213 netic field during the time period corresponding to the sharp increase of northward com-
 214 ponent B_z (defined as the period between the minimum and the maximum values) for
 215 all selected DF events. As MMS satellites are separated at electron scales, MVAB ap-
 216 plied on each single spacecraft magnetic field data gives similar *LMN* frames. *LMN* co-
 217 ordinates are well defined and correspond to *L* directed northward, *M* approximately
 218 directed downward, and *N* approximately directed Earthward. The time periods used
 219 to perform MVAB and its results are found in the supplementary material.

220 From these MVAB results, we define *L*, *M*, and *N* vectors as maximum, interme-
 221 diate, and minimum variance directions respectively. We have verified that the ratio be-
 222 tween the three corresponding eigenvalues, $\lambda_1, \lambda_2, \lambda_3$ are sufficiently large (average val-
 223 ues of the ratio $\lambda_M/\lambda_N \sim 22.034$ and of the ratio $\lambda_L/\lambda_N \sim 420.13$, lowest ratio value
 224 is 2.) indicating that the three directions are well separated.

225 The components of the normal vector are estimated by a timing analysis as well
 226 as the speed along the normal (these results can be found in the supplementary mate-
 227 rials). Note that in accordance with the propagation direction given by timing analy-
 228 sis, the orientation of the *N* vector of the MVAB was set to be positive (earthward) and
 229 *L* always oriented northward leading to *M* directed downward.

230 Figures 3A, B, C and D show the histogram for each component of the normal vec-
 231 tor (from TA and MVAB methods) as well as the magnitude of the normal speed ob-
 232 tained by TA. While all DFs are propagating earthward, percentages indicate that duskward/dawnward
 233 and northward/southward DF propagations are relatively balanced with no specific sta-
 234 tistically significant direction. Figure 3D shows a peak of the speed histogram around
 235 200 km/s. The smallest values below 50 km/s correspond to a normal orientation almost

perpendicular to the X axis when DFs are crossed through their flanks. In such a configuration, the DF speed can be much slower than the radial fast flow propagation.

In the present study, Superposed Epoch Analysis (SEA) are performed using the State Estimation and Analysis in Python (SeaPy). Time series have been reorganized by setting the maximum of the magnetic field as a reference for the measurements t_0 and the duration of a time period (t_0-180, t_0+180). The mean, the median and the interquartile range are computed. Note that the median measure is less impacted by departures from normality (Morley et al., 2014).

3 Statistical overview of classical DF properties

In this section, we describe the results obtained using a SEA described in section 2, where we defined the representative time series by setting the maximum of B_L component of the magnetic field as a time reference for the measurements and we kept 180 s of data on each side of this time reference. Furthermore, each DF data is time averaged at 0.3 s in order to remove all fluctuations which are not consistent with the phenomenon time scale.

After the first SEA using the full set of DFs, we realized that an important dispersion was due to the existence of two different types of magnetic signatures satisfying the DF selection criteria. From this observation, we decided to split the DF set into two different classes and perform two separate SEAs. Thus, the statistical characteristics of DF events for these two different classes are shown separately, reducing the dispersion for each class.

Figure 4 shows SEA results in order to illustrate ion scale properties for both DF classes in their respective LMN frame obtained from MVAB. Figure 4A presents the most important DF characteristics; namely a sharp increase of the northward component of the magnetic field B_L showing a small decrease (dip) just before the front as reported by previous studies (e. g., Ohtani et al., 2004; Runov et al., 2009; Z. Yao et al., 2013; Schmid et al., 2015; Z. H. Yao et al., 2015; C. M. Liu et al., 2018; Panov et al., 2022). Figure 4B shows the decrease of the electron density N_e to 0.21 p.cm^{-3} . Figures 4C, D display electron and ion pressure variations respectively. For electrons as well as for ions, the DF crossing always corresponds to a transition between a high pressure to a low pressure region on the largest scale (fluid). Figures 4F, G present the perpendicular electron and ion temperatures from FPI data in order to compare with proton temperature from HPCA data Figure 4E. Due to their different upper energy limit 40 keV (resp. 30 keV) for HPCA (resp. for FPI-DIS), FPI-DIS ion moments, although having a faster time resolution, can be underestimated. Indeed, a comparison of Figures 4G, E confirms that isotropic HPCA proton temperatures are much larger than FPI perpendicular ion temperatures (adding parallel ion temperatures to compute isotropic FPI temperatures does not compensate for the discrepancy, not shown). For the same reason, HPCA proton velocities $V_{H^+,N}$ are much larger than FPI ion velocities V_N as shown in Figures 4H, I. The V_N decreases shown by FPI-DIS within the front when ions are energized can also be considered as an artefact caused by this limited upper energy and not as a real reduction of the fast flow velocity.

Class I corresponds to 74.4% of selected DFs and has typical DF properties reported so far by previous statistical studies (e. g., Ohtani et al., 2004; Schmid et al., 2015; Huang et al., 2015; Schmid et al., 2019; Zhong et al., 2019). This DF class displays a slow decrease of the magnetic field after the front (see Figure 4(class I-[A])) and is associated with a lower ion velocity than class II (see Figures 4(class I-[H]&class II-[H])). They seem to propagate through a hotter plasma as ion and electron temperatures are higher before the front than for class II (see Figures 4(class I-[E,F,G]& class II-[E,F,G])). The ion perpendicular temperature increase is smaller whereas a significant ($\sim 50\%$) electron

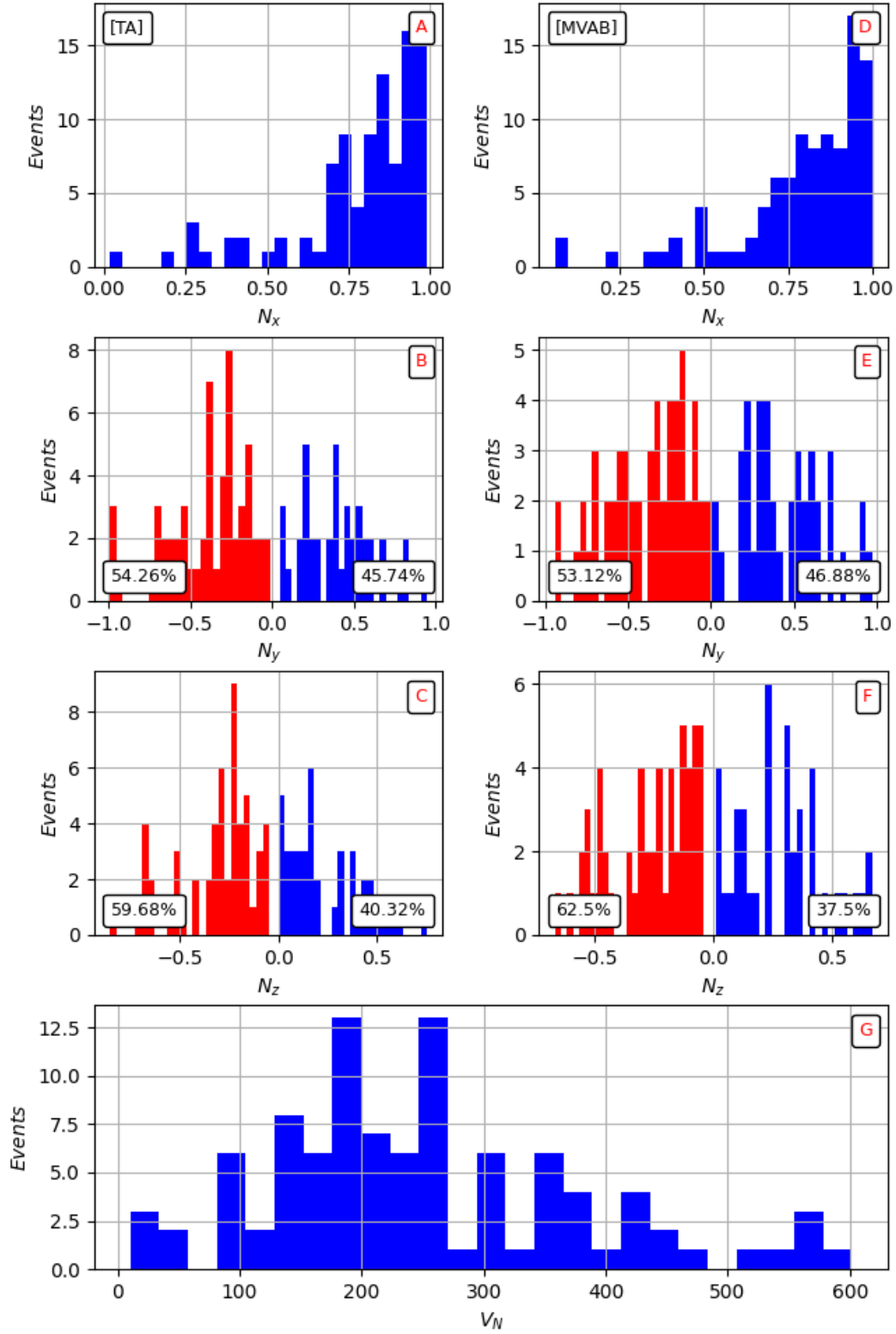


Figure 3. Histograms of the normal components in *GSE*, from TA panels (A), (B) and (C) and from MVAB panels (D), (E), and (F). Panel (G) shows the magnitude of the normal velocity obtained by TA.

perpendicular temperature increase is present. Yet, both pressures decrease monotonously at the DF (Figures 4(class I-[C,D])). This class is very similar to the decaying field pile-up event defined by H. S. Fu, Khotyaintsev, Vaivads, André, Sergeev, et al. (2012) although it is not clear that the peak of the velocity is collocated with the DF.

Class II corresponds to 25.6% of selected DFs. This new DF class has the same time scale for the rising and the falling of B_L (like a bump) (see Figure 4(class II-[A])) associated with minimums of density and (ion and electron) pressures (see Fig.4(class II-[B-D])). In addition to the pressure minimums at DF crossing, compressional fluctuations with smaller amplitudes are present. This DF class has faster velocity than class I (see Figure 4(class I-[H] and class II-[H])). As the $V_{H^+,N}$ maximum is located behind the front, this class could correspond to the growing field pile-up event defined by H. S. Fu, Khotyaintsev, Vaivads, André, Sergeev, et al. (2012). As already mentioned, these DF events seem to propagate through a colder plasma than class I as ion and electron temperatures before the front are smaller. Finally, both ion and electron perpendicular temperatures increase significantly ($\sim 50\%$). It is worth noting that this DF class is mostly detected on the duskside and includes all six DF events analyzed in Alqeeq et al. (2022) (see Figure 5(class II)). Substorm onsets being also more frequent in this region, it could suggest a possible link between the two phenomena.

Figure 5 displays an overview of class I and class II events that match the selection criteria. The colors represent the change in the northward magnetic field component $\langle B_z \rangle$ averaged over the full DF time interval, the arrows represent the DF normal speed perpendicular to the boundary (obtained by TA) projected onto the X/Y plane in GSE . While for class I, locations and propagations are relatively random, class II DFs have preferentially duskward locations and propagations with larger speeds.

Finally, Figure 6 shows that both classes are detected more frequently farther from the Earth ($\sim 24 - 25 R_E$). However, class I DF events can be also detected closer to the Earth down to $12 R_E$ while class II are only detected at farther distances.

Schmid et al. (2019) also identified two subcategories of DFs based on the sign of the magnetic dip preceding the DF. This dip property also permits us to distinguish between our two classes as class I shows an average and median positive B_L dips whereas class II shows slightly negative values (see Figures 4A). The histogram of the radial distance of our two DF categories, although more extended in distance from 12 to $26 R_E$, is globally consistent with theirs (see Figure 5 of Schmid et al. (2019)) where they found that positive dip DF category is detected closer to the Earth ($\sim 18 R_E$) than negative category ($\sim 26 R_E$). However, we do not find a decrease of the occurrence of the class I with the increase of the radial distance from the Earth. Furthermore, our class II has a larger median speed by a factor 2 than class I while Schmid's negative DF-dip subcategory has only a larger median speed by 50% than the positive DF-dip subcategory. Finally, the bump profile of our class II is not found for the Schmid's negative dip DF subcategory. Therefore, although sharing common properties, these two subclasses do not seem to be identical.

4 Currents density structure associated with DF

Following the same approach as for analyzing the first 6 DF events described in Alqeeq et al. (2022), we have compared the current densities computed from ion and electron moments averaged over the four individual spacecraft with those estimated independently from the magnetic field data at the same time resolution (0.3 s) using the curlometer technique (e. g., Chanteur & Harvey, 1998).

Figure 7 shows the SEA of the current densities computed from particle measurement $\mathbf{J}_{part} = en_e(\mathbf{v}_i - \mathbf{v}_e)$ (panel E) and computed from the magnetic field $\mathbf{J}_{curl} = (\nabla \times \mathbf{B})/\mu_0$ (panel D) estimated for each DF event in their own LMN frame. For both

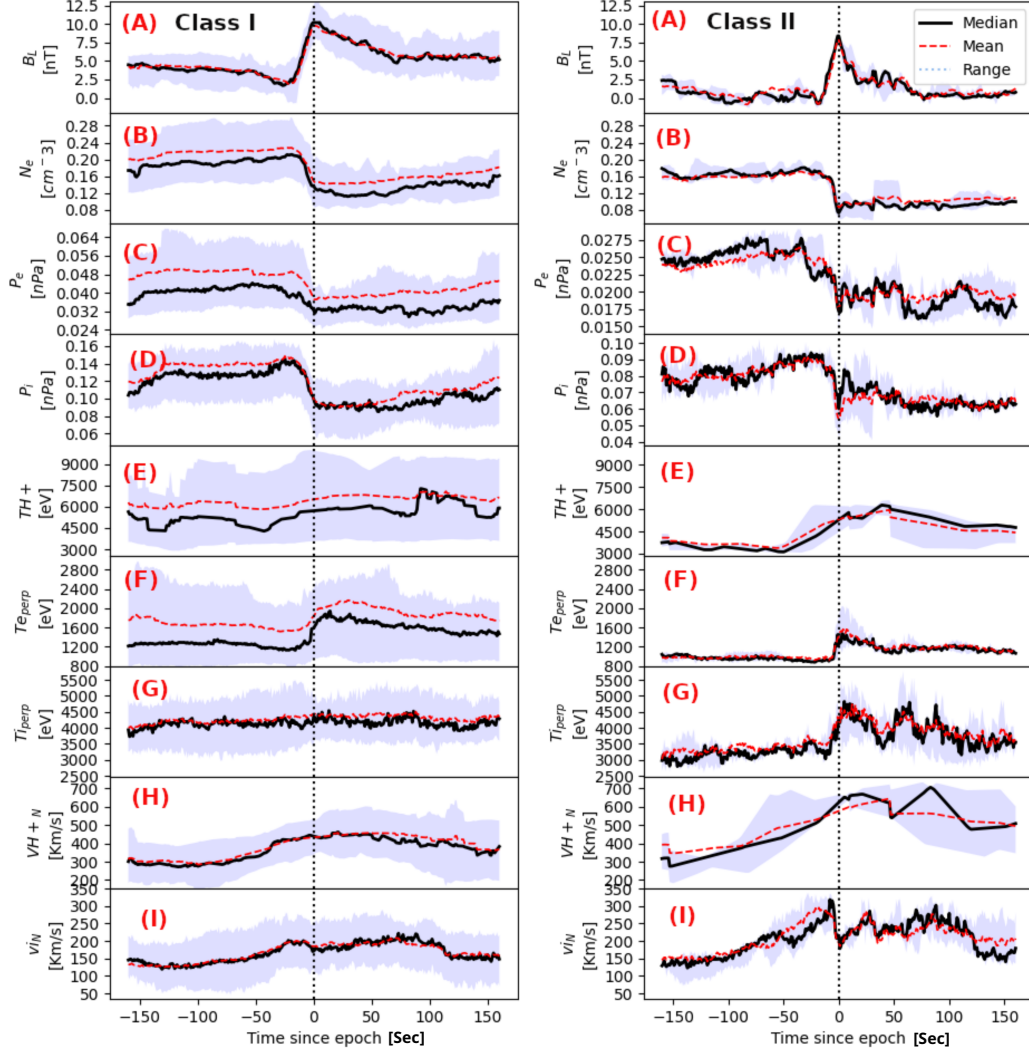


Figure 4. Superposed epoch analysis plots of DF signatures using 132 DFs, in their respective *LMN* frame, all data being time averaged at 0.3 s. In each panel, the black line marks the superposed epoch median, the red dashed line marks the superposed epoch mean, and the blue fill marks the interquartile range. (A) Magnetic field B_L , (B) electron density N_e , (C) and (D) electron and ion pressures from FPI, (E) HPCA proton temperature T_{H^+} , (F) and (G) perpendicular electron T_{perp}^e and ion T_{perp}^i temperatures from FPI, (H) HPCA normal proton bulk velocity V_{H^+N} , (I) FPI normal ion bulk velocity v_{iN} .

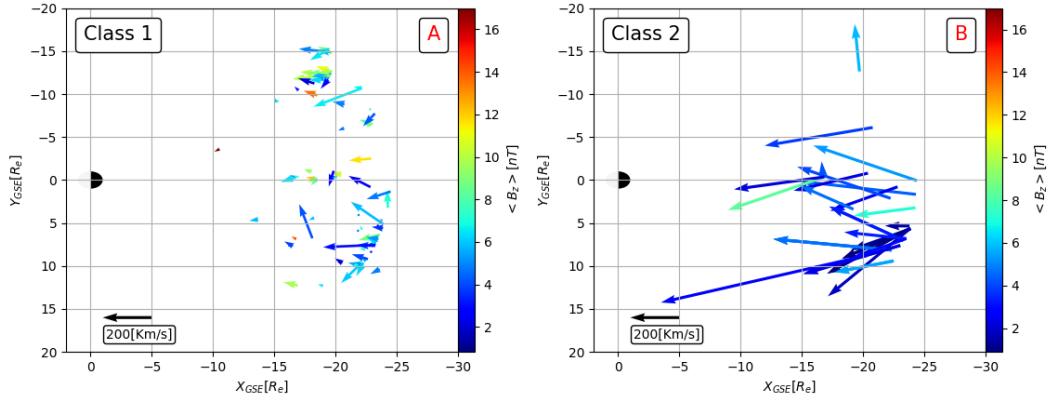


Figure 5. An overview of class I and class II events that match the selection criteria. The colors represent the change in the northward magnetic field component $\langle B_z \rangle$ time averaged over the full DF time interval, and the arrows represent the DF velocity perpendicular to the boundary (obtained by TA), projected onto the XY plane in GSE .

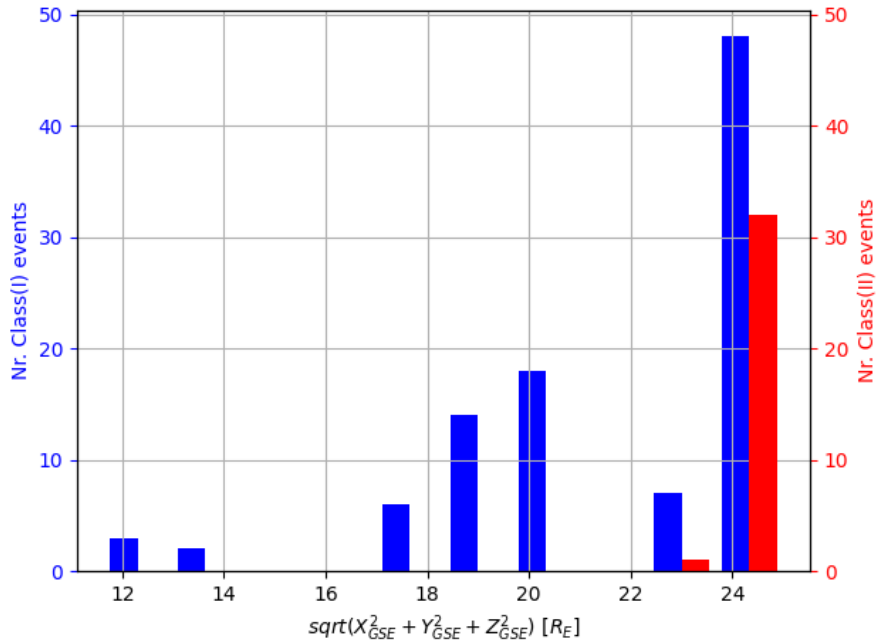


Figure 6. Histogram of the radial distance of the DF observation location. The red bars represent class(II) and the blue bars the class(I).

336 categories, the comparisons demonstrate good agreements between the two current density
 337 measurements although the values are quite small (~ -6 nA/m²). Note that each
 338 DF can be identified by its negative peak in J_M (an increase of cross-tail duskward current)
 339).

340 In addition to these measured current densities, one can obtain, from two-fluid theory,
 341 the diamagnetic current densities computed from the electron and ion pressure gradients.
 342 Due to the very low density in the magnetotail, the full divergence of the pressure
 343 tensor is very noisy and not reliable. However, these gradients along the DF normal
 344 can be estimated by a single satellite method by converting time evolution to distances
 345 using the DF speed obtained by timing analysis: $\partial_t P = \partial_N P_{i,e} \cdot V_N$. The M
 346 component of the total (perpendicular) diamagnetic current density becomes $J_{dia-tot,M} =$
 347 $B_L/B^2 \nabla_N (P_e + P_i)$ (where all data are averaged over the four satellites) and can be
 348 compared with the two other current densities computed from particle moments and cur-
 349 lometer technique.

350 Figures 7A, B and C show the electron diamagnetic current $J_{dia-e,M} = B_L/B^2 \nabla_N P_e$,
 351 the ion diamagnetic current $J_{dia-i,M} = B_L/B^2 \nabla_N P_i$, and the total diamagnetic cur-
 352 rent $J_{dia-tot,M} = B_L/B^2 \nabla_N (P_e + P_i)$ along the M direction, respectively. From the
 353 comparison between ion and electron diamagnetic currents, we see that for both classes
 354 the ion contribution is dominant and constitutes $\simeq 72$ % of the total diamagnetic cur-
 355 rent. Furthermore, for both classes, the total diamagnetic current along M is highly con-
 356 sistent with the curlometer and particle measurements indicating that the diamagnetic
 357 effect is the main source of the current. More importantly, the reversal in the current
 358 density pointed out in (Alqeeq et al., 2022) as the cause of the reversal of the energy con-
 359 version process for the 6 analysed DF events is confirmed by this statistical study as be-
 360 ing a common signature of class II events. Finally, this statistical study demonstrates
 361 that the reversal of the current density for class II events is mainly due to the reversal
 362 of the ion pressure gradient or in other words by the ion diamagnetic current. Although
 363 the electron density gradient follows the same behaviour, the electron pressure gradient
 364 is smaller mainly due to their smaller temperature. Therefore for both DF classes, the
 365 perpendicular current density structure of DF is governed by the diamagnetic current
 366 density dominated by the ion gradient pressure produced by the propagation of the fast
 367 flow through the magnetotail.

368 5 Statistical analysis of Ohm's Law

369 In this section, we reproduce the analysis of the different terms of the generalized
 370 Ohm's law for our two different DF classes. Figure 8 shows for both categories the SEA
 371 of the ideal ion frozen-in ($\mathbf{E}'^i = \mathbf{E} + \mathbf{v}_i \times \mathbf{B}$) and the Hall electric field ($\mathbf{J}_{part} \times \mathbf{B} / (en)$)
 372 terms in LMN coordinates. One can notice that for both classes the ideal ion frozen-
 373 in condition is mostly broken along the N axis ($E'_N{}^i \sim 3$ mV/m, panels D) whereas in
 374 contrast it is still well satisfied along L ($|E'_L{}^i| < 0.6$ mV/m, panels B). This behaviour
 375 is consistent with the idea of a front structure having a smaller (ion) scale in the direc-
 376 tion of propagation (N) perpendicular to the background magnetic field than along it
 377 (L). However, a significant peak (both for median and average) of ($E'_M{}^i \sim 1.8$ mV/m,
 378 right-hand panel C) is obtained for class II. This field is in the opposite direction of the
 379 M component of the Hall field (median value ~ -1.6 mV/m, right-hand side panel F)
 380 suggesting that the contribution from the electron pressure gradient would be quite large
 381 (~ 3.4 mV/m). As the median and mean values have opposite sign due to 2 extreme
 382 events, if we use the mean value ($\sim +0.8$ mV/m), the contribution of the electron pres-
 383 sure gradient would be only (~ 1 mV/m). These significant values of the electron pres-
 384 sure gradient along M could suggest that class II DFs have a smaller azimuthal scale (cross-
 385 tail direction) along M than class I DFs. Thus for both classes, in the N direction, ions
 386 are decoupled from the magnetic field mostly by the Hall electric field shown in panels
 387 G. However, for class II and in the M direction, the electron pressure gradient could con-

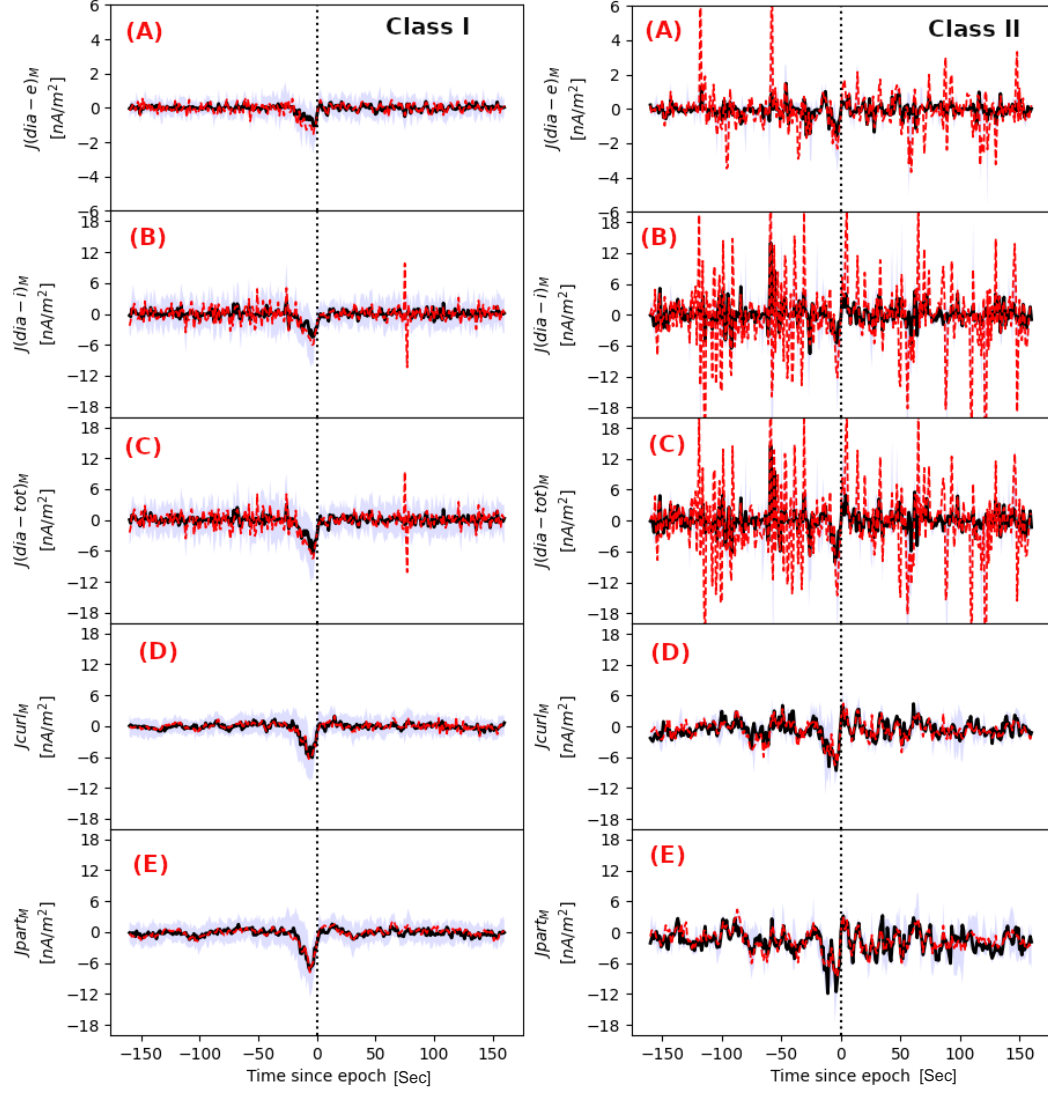


Figure 7. For both categories, superposed epoch analysis of the current densities along M calculated by using: (A) $J_{dia-e,M} = B_L/B^2 \nabla_N P_e$, (B) $J_{dia-i,M} = B_L/B^2 \nabla_N P_i$, (C) $J_{dia-tot,M} = B_L/B^2 \nabla_N (P_e + P_i)$, (D) $\mathbf{J}_{curl,M} = (\nabla \times \mathbf{B})/\mu_0$, (E) $\mathbf{J}_{part,M} = en_e(\mathbf{v}_i - \mathbf{v}_e)$. Same color code as Figure 4.

388 tribute significantly to ion decoupling. Furthermore, even in the N direction, the dis-
 389 crepancy between the two terms (ideal term and Hall field) can exceed $\simeq 1$ mV/m. This
 390 excess statistically confirms that the electron pressure gradient term is not negligible and
 391 reduce the positive Hall electric field along N despite the difficulty to estimate it from
 392 the four satellite measurements, see Figure 8(A).

393 Figure 9 shows for both categories, the SEA of the ideal electron frozen-in term ($\mathbf{E}'^e =$
 394 $\mathbf{E} + \mathbf{v}_e \times \mathbf{B}$) in LMN coordinates. Both ions and electrons are mostly magnetized along
 395 the L direction (panels B) as the ideal frozen-in term $|E'_L{}^e| < 0.8$ mV/m is about the
 396 electric field error bar although class II DFs are associated with larger fluctuations. In
 397 the N direction for class II DFs, electrons could be decoupled from the magnetic field
 398 as the departure to frozen-in condition ($E'_N{}^e \sim -1.6$ mV/m, right-hand side panel D)
 399 is consistent with the estimated electron pressure gradient term (right-hand side panel
 400 A) and assuming a non-zero curl of the electron pressure gradient term $-(\nabla P_e)/(en_e)$.
 401 This agreement is also found for class I DFs showing a bipolar signature but with smaller
 402 values ($E'_N{}^e \sim \pm 0.8$ mV/m, left-hand side panels D and A). In the M direction for which
 403 we are not able to estimate the electron pressure gradient, a larger departure to the ideal
 404 frozen-in condition is found for class II than for class I. This departure suggests, as from
 405 ion Ohm's law, that class II DFs could be more localized in the azimuthal (cross-tail)
 406 direction due to larger electron pressure gradients. Thus electrons could be decoupled
 407 from the magnetic field at DF by their pressure gradient term in the N direction and
 408 probably also in the M direction although it is not possible to confirm it using a single
 409 s/c method.

410 6 Energy conversion at DF

411 In this section, we present the results from the SEA of the energy conversion pro-
 412 cesses. For energy conversion, positive values of $\mathbf{j} \cdot \mathbf{E}$ correspond to an energy load or
 413 dissipation whereas negative values correspond to a generator or dynamo effect (e. g.,
 414 Birn & Hesse, 2005; Huang et al., 2015; Torbert et al., 2016; Alqeeq et al., 2022). Fig-
 415 ure 10 shows the results of the SEA of the energy conversion processes for our two DF
 416 categories. Figure 10A displays the magnetic component B_L for the context, Figure 10B
 417 the cross-tail electric field E_M , Figure 10C and D the energy conversion term in s/c frame
 418 $\mathbf{j} \cdot \mathbf{E}$ and in the electron frame $\mathbf{j} \cdot \mathbf{E}'$ respectively, and Figure 10E the current density
 419 J_{partM} computed from particle measurements shown again for reference. For both cat-
 420 egories, the SEA shows that, in the spacecraft frame Figure 10C, the energy is transferred
 421 from the electromagnetic fields to the plasma ($\mathbf{j} \cdot \mathbf{E} > 0$) ahead or at DF. This result
 422 is consistent with all previous DF studies. However, for class II as found for the 6 DF
 423 events by Alqeeq et al. (2022), a reversal of the energy conversion process is found be-
 424 hind the front. The energy is transferred from the plasma to the electromagnetic fields
 425 ($\mathbf{j} \cdot \mathbf{E} < 0$) due to the reversal of the ion diamagnetic current which has been confirmed
 426 in the previous section. Indeed, in Figure 10B, the M component of the electric field re-
 427 lated to the fast convective earthward plasma motion does not change sign. Therefore,
 428 for both classes, the energy conversion processes in the vicinity of DFs seem to be gov-
 429 erned by the ion pressure gradient generated by the flow propagation.

430 In the fluid frame Figure 10D, as found for the 6 DFs in (Alqeeq et al., 2022), the
 431 statistical study confirms that for both classes the energy is transferred from the plasma
 432 to the electromagnetic fields ($\mathbf{J} \cdot \mathbf{E}' < 0$, generator or dynamo) due to the contribu-
 433 tion of the electron pressure gradient in the Ohm's law and could lead to the slow down
 434 process of DFs during their earthward motion.

435 As in our 6 DF event study, we investigated the homogeneity of the energy con-
 436 version processes in the fluid frame observed around the DF. Indeed, from the 6 DF anal-
 437 ysis which all belong to class II, we have shown that the energy conversion process is not
 438 homogeneous at the scale of the tetrahedron (electron scales). We have found strong vari-

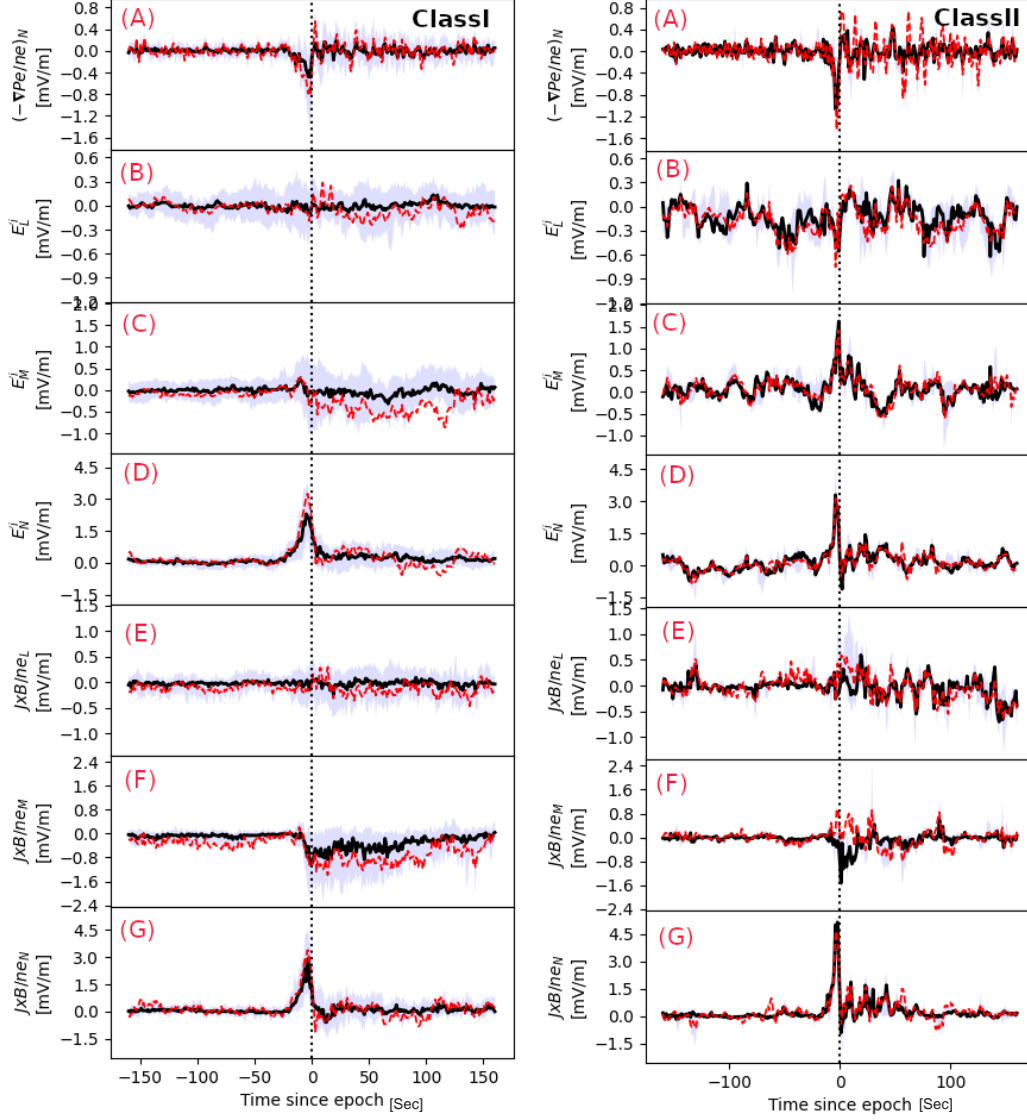


Figure 8. Superposed epoch analysis of the ion generalized Ohm's law comparison between different terms. Panel (A) includes the electron pressure gradient term along N . Panels (B), (C) and (D) shows L, M, N components of the electric field $\mathbf{E}' = \mathbf{E} + \mathbf{v}_i \times \mathbf{B}$ and panels (E), (F) and (G) shows L, M, N components of the Hall electric field $\mathbf{J}_{part}/(en_e)$, all data being time averaged at 0.3 s. Same color code as Figure 4.

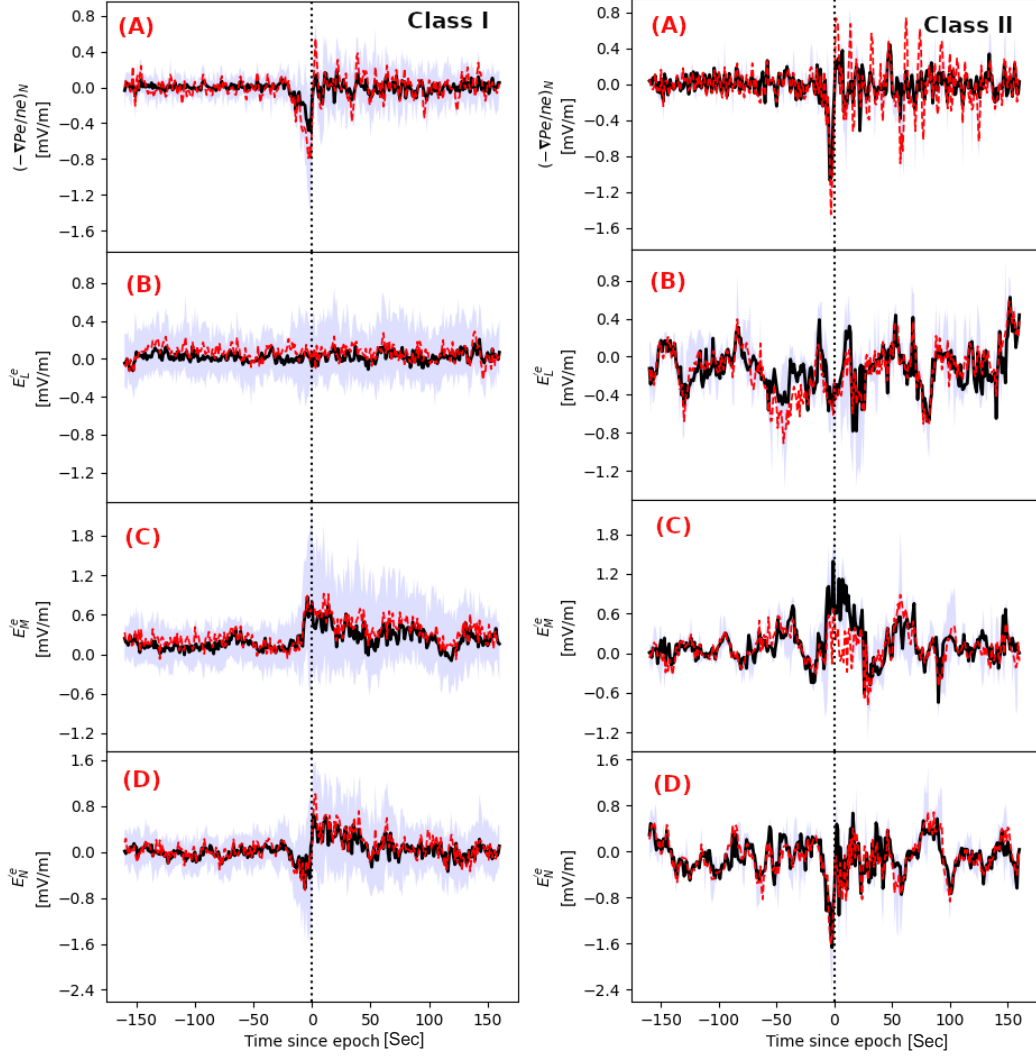


Figure 9. Superposed epoch analysis of the electron generalised Ohm's law comparison between different terms. Panel (A) includes the electron pressure gradient term along N . Panels (B), (C) and (D) shows L , M , N components of the electric field $\mathbf{E}' = \mathbf{E} + \mathbf{v}_e \times \mathbf{B}$, all data being time averaged at 0.3 s. Same color code as Figure 4.

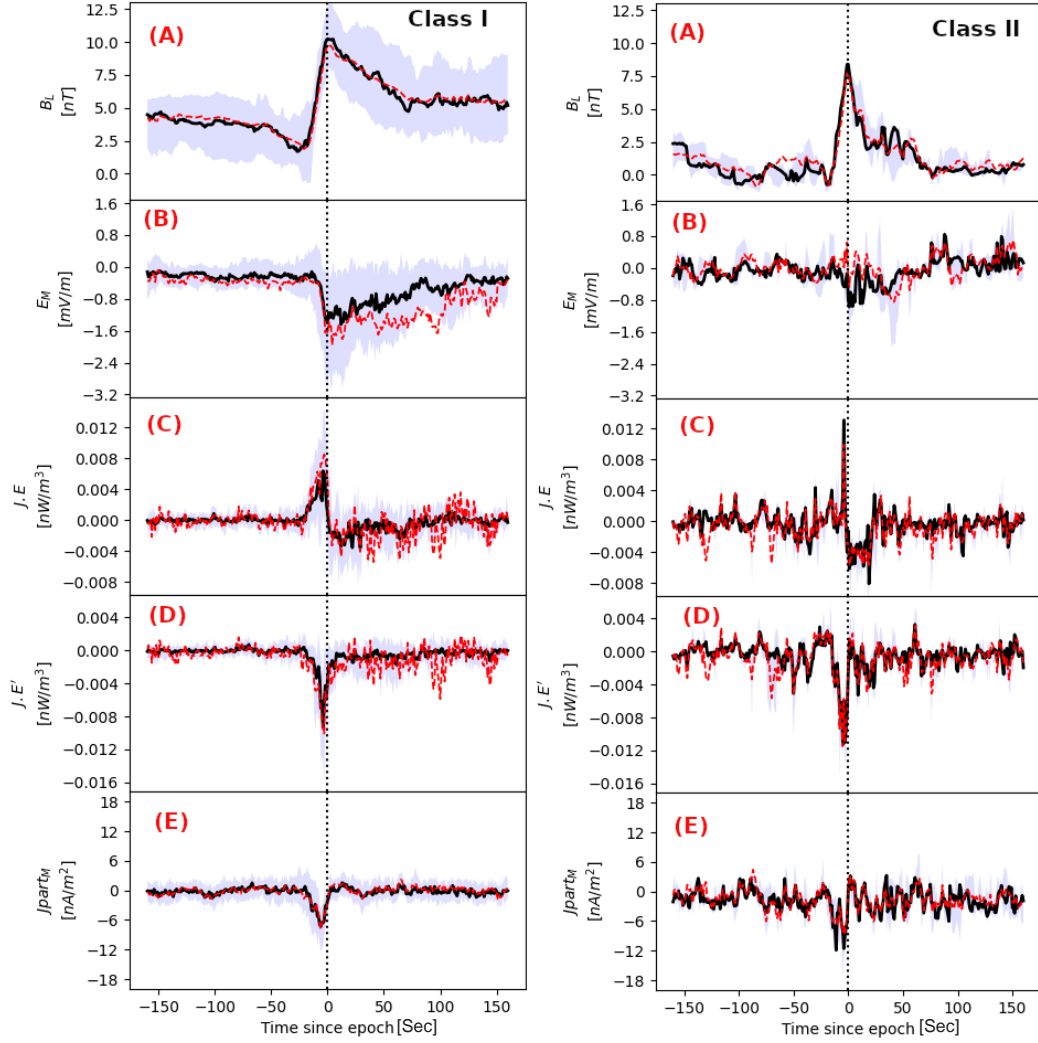


Figure 10. Superposed epoch plots of the energy conversion processes. (A) the magnetic field B_L , (B) the electric field E_M , (C) the energy conversion term in s/c frame $\mathbf{j} \cdot \mathbf{E}$, (D) the energy conversion term in electron frame $\mathbf{j} \cdot (\mathbf{E} + \mathbf{v}_e \times \mathbf{B})$, and (E) the current density J_{part_M} . Same color code as Figure 4.

439 ations of the sign and the amplitude of the energy conversion term obtained from one
 440 satellite to another. Such variations suggested that a physical process is going on at the
 441 electron scales while the DF is propagating earthward. Based on our estimates of the
 442 standard deviation (SD) for each component of the current density and the electric field
 443 in the fluid frame ($\mathbf{E}' = \mathbf{E} + \mathbf{v}_e \times \mathbf{B}$) normalized by their respective error bar, which
 444 can be written as $SD(X)/\Delta X = \sqrt{\sum_{i=1}^4 (X_i - \langle X \rangle)^2 / 4} / \Delta X$ where $\langle X \rangle$ is the
 445 four spacecraft average of the X component and ΔX its respective estimated error bar,
 446 we have shown that the non homogeneity was caused mainly by the electric field fluc-
 447 tuations as discussed in Alqeeq et al. (2022) in detail. The SEA of the normalized SD
 448 of the electric field and the current density shown in Figure 11 confirms the dominant
 449 role of the electric field fluctuations in the variability of the energy conversion term. In-
 450 deed, for both classes, the SD of electric fields is about 1 for x and y components (pan-
 451 els A and B) whereas the SD of current densities is always smaller than 1 for all com-
 452 ponents.

453 7 Summary and discussion

454 We have reported on a statistical study based on 132 DFs detected by the MMS
 455 mission during the full magnetotail season of 2017 (end of April to end of August). We
 456 found that the 132 events can be subdivided into two categories mostly according to their
 457 DF-shape (magnetic field profile): class I with 98 events (74.4%) for which the DF-shape
 458 shows a slow decrease of the magnetic field after the DF and is associated with smaller
 459 ion velocity, class II with 34 events (25.6%) for which the DF-shape shows the same time
 460 scale for the rising and the falling of the magnetic field (a bump) associated with min-
 461 imums of ion and electron pressures and faster velocity as shown in Alqeeq et al. (2022)
 462 for 6 DF events. These two classes can be considered as subcategories of the Schmid's
 463 DF category A (Schmid et al., 2015) as they both correspond to a decrease of the den-
 464 sity and an increase of the temperature. Note that Schmid's DF category B was excluded
 465 of our selection by the criteria imposing a density decrease after the DF passage. Our
 466 two classes share the same property regarding the different sign of the magnetic dip pre-
 467 ceding the DF as the two DF-dip subcategories identified by Schmid et al. (2019). How-
 468 ever, our class II with negative dip has a larger median speed by a factor 2 than class
 469 I while Schmid's negative DF-dip subcategory only corresponds to an increase of 50%
 470 of their median speed compared with positive DF-dip subcategory. Furthermore, the bump
 471 profile of class II and its detection more located on the duskside are not found for their
 472 negative DF-dip subcategory. Finally, if their and our histograms of the radial distance
 473 of the DF location show that negative dip DFs are detected farther from the Earth (\sim
 474 $25R_E$) than positive dip DFs (18 R_E and 24 R_E in their study and ours respectively),
 475 we do not find a decrease in class I DF with increasing distance from the Earth as the
 476 peak of their appearance is very close to that of class II DFs. Schmid et al. (2019) showed
 477 that the negative DF-dip category was correlated with field-aligned currents and sug-
 478 gested that they could correspond to flux rope structures and/or localized guide field re-
 479 connection events. However, from our study, we identified flux rope signatures usually
 480 ahead of DF and for both subcategories.

481 For both categories, using a single s/c method, we found that along the cross-tail
 482 current direction ($-M$), the ion diamagnetic current density contribution to the total
 483 diamagnetic current is dominant ($\sim 72\%$). For both categories, the enhancement of the
 484 ion pressure gradient ahead of the DF leads to an increase of the diamagnetic cross-tail
 485 current and to energy dissipation ($\mathbf{J} \cdot \mathbf{E} > 0$) in the spacecraft frame i.e. an energy trans-
 486 fer from the electromagnetic field to the plasma. This result related to the DF contri-
 487 bution to the global energy dissipation process in the magnetosphere is consistent with
 488 previous statistical analysis (e. g., Zhong et al., 2019; Song et al., 2020; Wang et al., 2020).
 489 However, for our new class II, we have found a reversal of the energy conversion term.
 490 This reversal is mainly produced by the reversal of the ion pressure gradient i.e. a re-

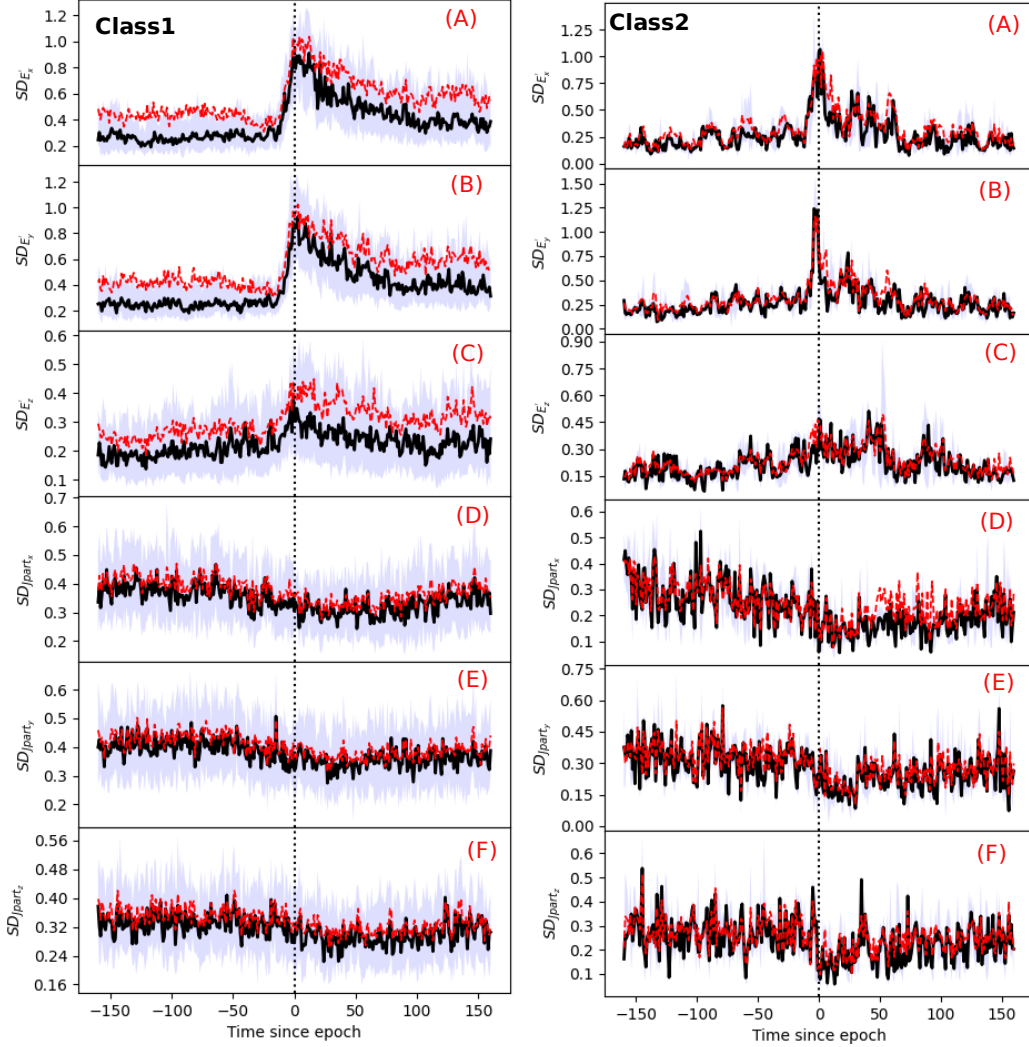


Figure 11. Superposed epoch analysis of the SD of class I and class II for each component of the current density and the electric field in the fluid frame ($\mathbf{E}' = \mathbf{E} + \mathbf{v}_e \times \mathbf{B}$) in *GSE*, all data being time averaged at 0.3 s. For context, panel (A) the $SD(E'_x)$, (B) the $SD(E'_y)$, (C) the $SD(E'_z)$, (D) the $SD(Jpart_x)$, (E) the $SD(Jpart_y)$, and (F) the $SD(Jpart_z)$. Same color code as Figure 4

491 versal of their diamagnetic current as the main component along M of the electric field
 492 due to the fast earthward plasma motion does not change sign. Therefore for class II DF
 493 events, the energy is transferred from the plasma to the electromagnetic field behind the
 494 front ($\mathbf{J} \cdot \mathbf{E} < 0$, dynamo effect). This reversal of the energy conversion term with sim-
 495 ilar values raises the question of a net contribution to the energy dissipation from this
 496 class of DF which still represents about 1/4 of the DF events. It raises also the question
 497 about the cause of this different behaviour compared with class I.

498 In the fluid frame and for both categories, we found that the energy is mostly trans-
 499 ferred from the plasma to the electromagnetic field ($\mathbf{J} \cdot \mathbf{E}' < 0$) ahead or at the DF
 500 which could contribute to the deceleration of the flow. As we have seen from the gen-
 501 eralized Ohm's law analysis, the non-ideal electric field comes from the electron pressure
 502 gradient. The latter, although contributing little to the total diamagnetic current due
 503 to the lower temperature of electrons, could lead to the electron decoupling at the front
 504 (assuming that the electron pressure does not depend only on the density and a non-zero
 505 curl of the electron pressure gradient term $-(\nabla P_e)/(en_e)$), see (Sittler & Scudder, 1980))
 506 for discussion and to a net energy conversion to the electromagnetic field. Thus, the en-
 507 ergy conversion process in the vicinity of DFs seems to be mainly controlled by the par-
 508 ticle pressure gradients: in the spacecraft frame, the contribution of the ion pressure gra-
 509 dient to the diamagnetic cross-tail current is dominant and determines the nature of the
 510 conversion process (dissipation versus dynamo) as the motional electric field does not
 511 change sign; in the fluid frame the electron pressure gradient, although weaker than that
 512 of the ions due to the lower temperature of electrons, could be sufficient to lead to the
 513 decoupling of electrons and to a net energy transfer from the plasma to the electromag-
 514 netic field. This transfer could result to the slowdown of the fast flows.

515 Furthermore, we have shown that the SEA of the generalized Ohm's law for all events
 516 confirms that the ideal frozen-in condition is broken for ions mostly due to the Hall elec-
 517 tric field ($\mathbf{J} \times \mathbf{B}/(en)$). We have seen that this field is produced by the enhancement
 518 of the cross-tail current caused by the ion pressure gradient at DF and the correspond-
 519 ing diamagnetic current but the electron pressure gradient although smaller also con-
 520 tributes. Electrons remain almost always magnetized except maybe at the front where
 521 a significant electron pressure gradient is found (assuming that the electron pressure does
 522 not depend only on the density). Finally, we have statistically examined the homogene-
 523 ity of the energy conversion processes in the fluid frame by estimating the standard de-
 524 viation of the current density and of the electric field measurements. For both categories,
 525 we found that the non-homogeneity comes from the variations of the electric field which
 526 occur at electron (tetrahedron) scales. These variations are produced by variations in
 527 the electron pressure gradient which are likely caused by a kinetic scale process. From
 528 the 6 DF analysis, we have suggested that this process could be identified as the lower-
 529 hybrid drift instability whose energy source lies in the enhancement of the pressure gra-
 530 dient ahead of the front as reported from observations and simulations (e. g., Sergeev
 531 et al., 2009; Divin, Khotyaintsev, Vaivads, & André, 2015; Divin, Khotyaintsev, Vaivads,
 532 André, Markidis, & Lapenta, 2015; Hosner et al., 2022).

533 The identification of the class II DFs raises many new questions:

- 534 • Why and how are they produced compared with the typical class I?
- 535 • Why are they mostly detected on the duskside?
- 536 • Why are they observed less often?
- 537 • What is their net contribution to the global circulation of magnetospheric energy?

538 We do not pretend here to answer all these new questions but we want to suggest some
 539 clues. The duskside near-Earth magnetotail (pre-midnight sector) has been known for
 540 a long time to be a preferential location for substorm onset (e. g., Nagai et al., 1998; Baumjo-
 541 hann et al., 1999; Angelopoulos et al., 2008, 2013) or/and magnetotail reconnection (e.

542 g., Sitnov et al., 2009; Zhou et al., 2011; Runov et al., 2012; H. S. Fu et al., 2013; Drake
 543 et al., 2014; Lu et al., 2019). Therefore, class II DF events could be directly related to
 544 onset events although it has been shown that fast flows and DF can be detected with-
 545 out substorms (e. g., Lui, 2001; Runov et al., 2009, 2011b). Class II DFs would be de-
 546 tected near the substorm onset with an higher probability in the pre-midnight sector but
 547 with a lower probability than fast flow detection anywhere across the magnetotail. This
 548 conjecture could be tested in the future by investigating the occurrence of substorm on-
 549 set with regard to class II events.

550 Recently combining THEMIS observations and 3D PIC simulations, Panov et al.
 551 (2022) identified ion gyroradius scale structures associated with the propagation of heads
 552 produced by the non-linear evolution of the kinetic Ballooning-Interchange Instability
 553 (BICI). The BICI head structures correspond to the sharp increase of the northward com-
 554 ponent of the magnetic field and the decrease of the density (e. g., Pritchett et al., 2014).
 555 They were detected by the three THEMIS near-Earth probes when they were located
 556 between -7.5 and $-7.9 R_E$ therefore much closer to the Earth than DFs detected by MMS.
 557 Their measurements were performed in a stronger magnetic field (~ 60 nT) and farther
 558 from the equator ($B_x \sim 40$ nT). Furthermore, the heads were moving downward while
 559 on each head side plasma was moving tailward leading to a flow reversal during the head
 560 crossing by the probes. However, some properties pointed out by Panov *et al.* could have
 561 some similarities with properties of class II DFs. The BICI head crossing is associated
 562 with a density trough and a hump of the ion temperature in addition to the classical DF
 563 signature (B_z increase up to 40 nT preceded by a negative dip and $V_x \sim 400$ km/s) as
 564 for class II. The authors used the spacecraft potential with a time resolution of $1/128 \sim$
 565 0.008 s to estimate the density and to show the density trough. as THEMIS spin res-
 566 olution (3 sec) of particle moments is not sufficient. Moreover, while from THEMIS mea-
 567 surements the authors showed that the ion temperature increases by a factor 2 on the
 568 duskside of the head, in our MMS measurements we found only an increase $\sim 50\%$. They
 569 attributed the enhancement of the ion temperature on the duskside of the head to the
 570 penetration of the suprathermal ions from the dawnside across the head to the duskside.
 571 This process could be also investigated in the future from our DF database. Despite these
 572 differences, BICI head crossing appears to be a good candidate to interpret our class II
 573 DFs. However taking into account the different locations between THEMIS and MMS
 574 observations, class II DFs could correspond to BICI head crossings in the early stages
 575 of their development before they were slowed down and broadened closer to the Earth
 576 due to the interaction with the stronger dipole field.

577 8 Conclusion

578 From a statistical study based on MMS data gathered during the full magnetotail
 579 season of 2017, we have identified two DF subcategories mostly according to their DF-
 580 shape (magnetic field profile): class I (74.4%) showing a slow decrease of the magnetic
 581 field after the DF and associated with smaller ion velocity, class II (25.6%) showing the
 582 same time scale for the rising and the falling of the magnetic field (a bump) associated
 583 with minimums of ion and electron pressures and faster velocity. For both categories,
 584 the ion diamagnetic current density contribution to the total diamagnetic current is dom-
 585 inant ($\sim 72\%$) and lead to an energy dissipation ($\mathbf{J} \cdot \mathbf{E} > 0$) ahead of the DF i.e. an
 586 energy transfer from the electromagnetic field to the plasma. However, class II presents
 587 a reversal of the energy conversion term after the DF. This reversal is mainly produced
 588 by the reversal of the ion pressure gradient i.e. a reversal of their diamagnetic current
 589 as the main component along M of the electric field due to the fast earthward plasma
 590 motion does not change sign. Therefore, the energy is transferred from the plasma to
 591 the electromagnetic field behind the front ($\mathbf{J} \cdot \mathbf{E} < 0$, dynamo effect). In the fluid frame
 592 and for both categories, we found that the energy is mostly transferred from the plasma
 593 to the electromagnetic field ($\mathbf{J} \cdot \mathbf{E}' < 0$) ahead or at the DF which could contribute to

594 the deceleration of the flow. Ions are found to be decoupled from the magnetic field along
 595 the normal direction at DF mainly due to the Hall electric field although the electron
 596 pressure could contribute too. Electrons could be also decoupled at DF by the effect of
 597 their electron pressure gradient assuming a non-zero curl of the electron pressure gra-
 598 dient term $-(\nabla P_e)/(en_e)$, i.e a pressure not depending only on the density. Although
 599 sharing common properties with the two subcategories identified by Schmid et al. (2019)
 600 based on the sign of the magnetic dip preceding the DF, our classe II DF shows impor-
 601 tant distinct features: a magnetic bump profile, faster speed and location on the dusk-
 602 side. Schmid et al. (2019) suggested that their negative dip DF events could be related
 603 to flux ropes or localized reconnection events with guide field. Although our study does
 604 not rule out these suggestions, we did not find more flux rope signatures associated with
 605 our class II than class I. We suggest that class II DF events could be also related to BICI
 606 head crossings described by Panov et al. (2022). Further investigations are therefore still
 607 necessary to better understand the nature and the contribution to the global energy cy-
 608 cle of the different classes of DFs moving towards the Earth through the magnetotail.
 609

610 Acknowledgments

611 We thank the entire MMS team for providing data publicly available from the MMS Sci-
 612 ence Data Center (<http://lasp.colorado.edu/mms/sdc/public/>), the spedas software team (Angelopoulos
 613 et al., 2019) in particular E. Grimes for pyspedas effort developments and the AIDApv
 614 software team (Lapenta & AIDA H2020 Team, 2019). S.W. Alqeeq’s PhD fellowship is
 615 supported by CNES and PAUSE program ([https://www.college-de-france.fr/site/programme-
 616 pause/index.htm](https://www.college-de-france.fr/site/programme-pause/index.htm)), managed by CNRS.

617 References

- 618 Alqeeq, S. W., Le Contel, O., Canu, P., Retinò, A., Chust, T., Mirioni, L., ...
 619 Lavraud, B. (2022, January). Investigation of the homogeneity of energy
 620 conversion processes at dipolarization fronts from MMS measurements. *Physics
 621 of Plasmas*, *29*(1), 012906. doi: 10.1063/5.0069432
- 622 Angelopoulos, V. (2008, December). The THEMIS Mission. , *141*(1-4), 5-34. doi: 10
 623 .1007/s11214-008-9336-1
- 624 Angelopoulos, V., Baumjohann, W., Kennel, C. F., Coroniti, F. V., Kivelson, M. G.,
 625 Pellat, R., ... Paschmann, G. (1992, April). Bursty Bulk Flows in the Inner
 626 Central Plasma Sheet. , *97*(A4), 4027-4039. doi: 10.1029/91JA02701
- 627 Angelopoulos, V., Cruce, P., Drozdov, A., Grimes, E. W., Hatzigeorgiu, N.,
 628 King, D. A., ... Schroeder, P. (2019, January). The Space Physics En-
 629 vironment Data Analysis System (SPEDAS). , *215*(1), 9. doi: 10.1007/
 630 s11214-018-0576-4
- 631 Angelopoulos, V., Kennel, C. F., Coroniti, F. V., Pellat, R., Kivelson, M. G.,
 632 Walker, R. J., ... Gosling, J. T. (1994, November). Statistical characteristics
 633 of bursty bulk flow events. , *99*(A11), 21257-21280. doi: 10.1029/94JA01263
- 634 Angelopoulos, V., McFadden, J. P., Larson, D., Carlson, C. W., Mende, S. B., Frey,
 635 H., ... Kepko, L. (2008, August). Tail Reconnection Triggering Substorm
 636 Onset. *Science*, *321*(5891), 931. doi: 10.1126/science.1160495
- 637 Angelopoulos, V., Runov, A., Zhou, X. Z., Turner, D. L., Kiehas, S. A., Li,
 638 S. S., & Shinohara, I. (2013, September). Electromagnetic Energy Con-
 639 version at Reconnection Fronts. *Science*, *341*(6153), 1478-1482. doi:
 640 10.1126/science.1236992
- 641 Baumjohann, W., Hesse, M., Kokubun, S., Mukai, T., Nagai, T., & Petrukovich,
 642 A. A. (1999, November). Substorm dipolarization and recovery. , *104*(A11),
 643 24995-25000. doi: 10.1029/1999JA900282
- 644 Baumjohann, W., Paschmann, G., & Luehr, H. (1990, April). Characteristics of

- 645 high-speed ion flows in the plasma sheet. , *95*(A4), 3801-3809. doi: 10.1029/
 646 JA095iA04p03801
- 647 Birn, J., & Hesse, M. (2005, November). Energy release and conversion by reconnection
 648 in the magnetotail. *Annales Geophysicae*, *23*, 3365-3373. doi: 10.5194/
 649 angeo-23-3365-2005
- 650 Burch, J. L., Torbert, R. B., Phan, T. D., Chen, L.-J., Moore, T. E., Ergun, R. D.,
 651 ... Chandler, M. (2016). Electron-Scale Measurements of Magnetic Reconnec-
 652 tion in Space. *Science*. doi: doi:10.1126/science.aaf2939
- 653 Chanteur, G., & Harvey, C. (1998, July). Spatial interpolation fo four spacecraft:
 654 Application to magnetic gradients. In G. Paschman & P. Daly (Eds.), *Analysis*
 655 *Methods for Multi-Spacecraft Data* (p. 371-393). European Space Agency.
- 656 Divin, A., Khotyaintsev, Y. V., Vaivads, A., & André, M. (2015, February). Lower
 657 hybrid drift instability at a dipolarization front. *Journal of Geophysical Re-*
 658 *search (Space Physics)*, *120*(2), 1124-1132. doi: 10.1002/2014JA020528
- 659 Divin, A., Khotyaintsev, Y. V., Vaivads, A., André, M., Markidis, S., & Lapenta, G.
 660 (2015, April). Evolution of the lower hybrid drift instability at reconnection
 661 jet front. *Journal of Geophysical Research (Space Physics)*, *120*(4), 2675-2690.
 662 doi: 10.1002/2014JA020503
- 663 Drake, J. F., Swisdak, M., Cassak, P. A., & Phan, T. D. (2014, June). On the
 664 3-D structure and dissipation of reconnection-driven flow bursts. , *41*(11),
 665 3710-3716. doi: 10.1002/2014GL060249
- 666 Ergun, R. E., Tucker, S., Westfall, J., Goodrich, K. A., Malaspina, D. M., Summers,
 667 D., ... Cully, C. M. (2016, March). The Axial Double Probe and Fields
 668 Signal Processing for the MMS Mission. *Space Sci. Rev.*, *199*, 167-188. doi:
 669 10.1007/s11214-014-0115-x
- 670 Escoubet, C. P., Fehringer, M., & Goldstein, M. L. (2001). Introduction the cluster
 671 mission. *Annales Geophysicae*, *19*, 1197-1200.
- 672 Fu, H., Grigorenko, E. E., Gabrielse, C., Liu, C., Lu, S., Hwang, K. J., ... Chen,
 673 F. (2020, February). Magnetotail dipolarization fronts and particle ac-
 674 celeration: A review. *Science China Earth Sciences*, *63*(2), 235-256. doi:
 675 10.1007/s11430-019-9551-y
- 676 Fu, H. S., Cao, J. B., Khotyaintsev, Y. V., Sitnov, M. I., Runov, A., Fu, S. Y.,
 677 ... Huang, S. Y. (2013, December). Dipolarization fronts as a conse-
 678 quence of transient reconnection: In situ evidence. , *40*(23), 6023-6027. doi:
 679 10.1002/2013GL058620
- 680 Fu, H. S., Khotyaintsev, Y. V., Vaivads, A., André, M., & Huang, S. Y. (2012,
 681 March). Electric structure of dipolarization front at sub-proton scale. *Geophys.*
 682 *Res. Lett.*, *39*, L06105. doi: 10.1029/2012GL051274
- 683 Fu, H. S., Khotyaintsev, Y. V., Vaivads, A., André, M., Sergeev, V. A., Huang,
 684 S. Y., ... Daly, P. W. (2012, December). Pitch angle distribution of
 685 suprathermal electrons behind dipolarization fronts: A statistical overview.
 686 *Journal of Geophysical Research (Space Physics)*, *117*(A12), A12221. doi:
 687 10.1029/2012JA018141
- 688 Hamrin, M., Pitkänen, T., Norqvist, P., Karlsson, T., Nilsson, H., André, M., ...
 689 Dandouras, I. (2014, November). Evidence for the braking of flow bursts as
 690 they propagate toward the Earth. *Journal of Geophysical Research (Space*
 691 *Physics)*, *119*(11), 9004-9018. doi: 10.1002/2014JA020285
- 692 Hosner, M., Nakamura, R., Nakamura, T. K. M., Schmid, D., Panov, E. V., &
 693 Plaschke, F. (2022, January). Statistical investigation of electric field fluc-
 694 tuations around the lower-hybrid frequency range at dipolarization fronts
 695 in the near-earth magnetotail. *Physics of Plasmas*, *29*(1), 012111. doi:
 696 10.1063/5.0067382
- 697 Huang, S. Y., Fu, H. S., Yuan, Z. G., Zhou, M., Fu, S., Deng, X. H., ... Yu, X. D.
 698 (2015, June). Electromagnetic energy conversion at dipolarization fronts: Mul-
 699 tispacescraft results. *Journal of Geophysical Research (Space Physics)*, *120*(6),

- 700 4496-4502. doi: 10.1002/2015JA021083
- 701 Khotyaintsev, Y. V., Divin, A., Vaivads, A., André, M., & Markidis, S. (2017,
702 February). Energy conversion at dipolarization fronts. , *44*(3), 1234-1242. doi:
703 10.1002/2016GL071909
- 704 Lapenta, G., & AIDA H2020 Team. (2019, May). Processing big data from space
705 missions and massively parallel simulations within the Horizon 2020 Project
706 AIDA. In *Solar heliospheric and interplanetary environment (shine 2019)*
707 (p. 44).
- 708 Le Contel, O., Nakamura, R., Breuillard, H., Argall, M. R., Graham, D. B., Fis-
709 cher, D., ... Jaynes, A. N. (2017, December). Lower Hybrid Drift Waves and
710 Electromagnetic Electron Space-Phase Holes Associated With Dipolarization
711 Fronts and Field-Aligned Currents Observed by the Magnetospheric Multiscale
712 Mission During a Substorm. *Journal of Geophysical Research (Space Physics)*,
713 *122*(12), 12,236-12,257. doi: 10.1002/2017JA024550
- 714 Li, H., Zhou, M., Deng, X., Yuan, Z., Guo, L., Yu, X., ... Huang, S. (2015, Febru-
715 ary). A statistical study on the whistler waves behind dipolarization fronts.
716 *Journal of Geophysical Research (Space Physics)*, *120*(2), 1086-1095. doi:
717 10.1002/2014JA020474
- 718 Lindqvist, P.-A., Olsson, G., Torbert, R. B., King, B., Granoff, M., Rau, D.,
719 ... Tucker, S. (2016, March). The Spin-Plane Double Probe Elec-
720 tric Field Instrument for MMS. *Space Sci. Rev.*, *199*, 137-165. doi:
721 10.1007/s11214-014-0116-9
- 722 Liu, C. M., Fu, H. S., Xu, Y., Khotyaintsev, Y. V., Burch, J. L., Ergun, R. E., ...
723 Torbert, R. B. (2018, May). Electron-Scale Measurements of Dipolarization
724 Front. , *45*(10), 4628-4638. doi: 10.1029/2018GL077928
- 725 Liu, J., Angelopoulos, V., Runov, A., & Zhou, X.-Z. (2013, May). On the current
726 sheets surrounding dipolarizing flux bundles in the magnetotail: The case for
727 wedgelets. *Journal of Geophysical Research (Space Physics)*, *118*, 2000-2020.
728 doi: 10.1002/jgra.50092
- 729 Lu, S., Artemyev, A. V., Angelopoulos, V., Lin, Y., Zhang, X. J., Liu, J., ...
730 Strangeway, R. J. (2019, February). The Hall Electric Field in Earth's Mag-
731 netotail Thin Current Sheet. *Journal of Geophysical Research (Space Physics)*,
732 *124*(2), 1052-1062. doi: 10.1029/2018JA026202
- 733 Lui, A. T. Y. (2001, November). Current controversies in magnetospheric physics.
734 *Reviews of Geophysics*, *39*(4), 535-563. doi: 10.1029/2000RG000090
- 735 Morley, S., Koller, J., Welling, D., Larsen, B., & Niehof, J. (2014, January).
736 *SpacePy: Python-Based Tools for the Space Science Community*.
- 737 Nagai, T., Fujimoto, M., Saito, Y., Machida, S., Terasawa, T., Nakamura, R., ...
738 Kokubun, S. (1998, March). Structure and dynamics of magnetic reconnec-
739 tion for substorm onsets with Geotail observations. , *103*(A3), 4419-4440. doi:
740 10.1029/97JA02190
- 741 Nakamura, R., Baumjohann, W., Mouikis, C., Kistler, L. M., Runov, A., Volwerk,
742 M., ... Balogh, A. (2004, May). Spatial scale of high-speed flows in the plasma
743 sheet observed by Cluster. , *31*(9), L09804. doi: 10.1029/2004GL019558
- 744 Nakamura, T. K. M., Umeda, T., Nakamura, R., Fu, H. S., & Oka, M. (2019, De-
745 cember). Disturbance of the Front Region of Magnetic Reconnection Out-
746 flow Jets due to the Lower-Hybrid Drift Instability. , *123*(23), 235101. doi:
747 10.1103/PhysRevLett.123.235101
- 748 Ohtani, S.-I., Shay, M. A., & Mukai, T. (2004, March). Temporal structure of the
749 fast convective flow in the plasma sheet: Comparison between observations and
750 two-fluid simulations. *Journal of Geophysical Research (Space Physics)*, *109*,
751 A03210. doi: 10.1029/2003JA010002
- 752 Pan, D.-X., Khotyaintsev, Y. V., Graham, D. B., Vaivads, A., Zhou, X.-Z., André,
753 M., ... Burch, J. L. (2018, November). Rippled Electron-Scale Structure of a
754 Dipolarization Front. , *45*(22), 12,116-12,124. doi: 10.1029/2018GL080826

- 755 Panov, E. V., Lu, S., & Pritchett, P. L. (2022, February). Magnetotail Ion Structuring by Kinetic Ballooning-Interchange Instability. , *49*(3), e96796. doi: 10.1029/2021GL096796
- 756
757
- 758 Pollock, C., Moore, T., Jacques, A., Burch, J., Gliese, U., Saito, Y., ... Zeuch, M. (2016, March). Fast Plasma Investigation for Magnetospheric Multiscale. , *199*(1-4), 331-406. doi: 10.1007/s11214-016-0245-4
- 759
760
- 761 Pontius, J., D. H., & Wolf, R. A. (1990, January). Transient flux tubes in the terrestrial magnetosphere. , *17*(1), 49-52. doi: 10.1029/GL0171001p00049
- 762
- 763 Pritchett, P. L., & Coroniti, F. V. (2010, June). A kinetic ballooning/interchange instability in the magnetotail. *Journal of Geophysical Research (Space Physics)*, *115*(A6), A06301. doi: 10.1029/2009JA014752
- 764
765
- 766 Pritchett, P. L., Coroniti, F. V., & Nishimura, Y. (2014, June). The kinetic ballooning/interchange instability as a source of dipolarization fronts and auroral streamers. *Journal of Geophysical Research (Space Physics)*, *119*, 4723-4739. doi: 10.1002/2014JA019890
- 767
768
769
- 770 Richard, L., Khotyaintsev, Y. V., Graham, D. B., & Russell, C. T. (2022, November). Are Dipolarization Fronts a Typical Feature of Magnetotail Plasma Jets Fronts? , *49*(22), e2022GL101693. doi: 10.1029/2022GL101693
- 771
772
- 773 Runov, A., Angelopoulos, V., Sitnov, M. I., Sergeev, V. A., Bonnell, J., McFadden, J. P., ... Auster, U. (2009, July). THEMIS observations of an earthward-propagating dipolarization front. *Geophys. Res. Lett.*, *36*, L14106. doi: 10.1029/2009GL038980
- 774
775
776
- 777 Runov, A., Angelopoulos, V., & Zhou, X. Z. (2012, May). Multipoint observations of dipolarization front formation by magnetotail reconnection. *Journal of Geophysical Research (Space Physics)*, *117*(A5), A05230. doi: 10.1029/2011JA017361
- 778
779
780
- 781 Runov, A., Angelopoulos, V., Zhou, X. Z., Zhang, X. J., Li, S., Plaschke, F., & Bonnell, J. (2011a, May). A THEMIS multicase study of dipolarization fronts in the magnetotail plasma sheet. *Journal of Geophysical Research (Space Physics)*, *116*(A5), A05216. doi: 10.1029/2010JA016316
- 782
783
784
- 785 Runov, A., Angelopoulos, V., Zhou, X. Z., Zhang, X. J., Li, S., Plaschke, F., & Bonnell, J. (2011b, May). A THEMIS multicase study of dipolarization fronts in the magnetotail plasma sheet. *Journal of Geophysical Research (Space Physics)*, *116*(A5), A05216. doi: 10.1029/2010JA016316
- 786
787
788
- 789 Russell, C. T., Anderson, B. J., Baumjohann, W., Bromund, K. R., Dearborn, D., Fischer, D., ... Richter, I. (2016, March). The Magnetospheric Multiscale Magnetometers. *Space Sci. Rev.*, *199*, 189-256. doi: 10.1007/s11214-014-0057-3
- 790
791
792
- 793 Schmid, D., Nakamura, R., Plaschke, F., Volwerk, M., & Baumjohann, W. (2015, February). Two states of magnetotail dipolarization fronts: A statistical study. *Journal of Geophysical Research (Space Physics)*, *120*(2), 1096-1108. doi: 10.1002/2014JA020380
- 794
795
796
- 797 Schmid, D., Volwerk, M., Nakamura, R., Baumjohann, W., & Heyn, M. (2011, September). A statistical and event study of magnetotail dipolarization fronts. *Annales Geophysicae*, *29*(9), 1537-1547. doi: 10.5194/angeo-29-1537-2011
- 798
799
- 800 Schmid, D., Volwerk, M., Plaschke, F., Nakamura, R., Baumjohann, W., Wang, G. Q., ... Zhang, T. L. (2019, January). A Statistical Study on the Properties of Dips Ahead of Dipolarization Fronts Observed by MMS. *Journal of Geophysical Research (Space Physics)*, *124*(1), 139-150. doi: 10.1029/2018JA026062
- 801
802
803
804
- 805 Sergeev, V., Angelopoulos, V., Apatenkov, S., Bonnell, J., Ergun, R., Nakamura, R., ... Runov, A. (2009, November). Kinetic structure of the sharp injection/dipolarization front in the flow-braking region. , *36*(21), L21105. doi: 10.1029/2009GL040658
- 806
807
808
- 809 Sitnov, M. I., Merkin, V. G., Roytershteyn, V., & Swisdak, M. (2018, May). Kinetic

- 810 Dissipation Around a Dipolarization Front. , *45*(10), 4639-4647. doi: 10.1029/
 811 2018GL077874
- 812 Sitnov, M. I., Swisdak, M., & Divin, A. V. (2009, April). Dipolarization fronts as a
 813 signature of transient reconnection in the magnetotail. *Journal of Geophysical*
 814 *Research (Space Physics)*, *114*(A4), A04202. doi: 10.1029/2008JA013980
- 815 Sittler, J., E. C., & Scudder, J. D. (1980, October). An empirical polytrope law
 816 for solar wind thermal electrons between 0.45 and 4.76 AU: Voyager 2 and
 817 Mariner 10. , *85*(A10), 5131-5137. doi: 10.1029/JA085iA10p05131
- 818 Song, L., Zhou, M., Yi, Y., Deng, X., Zhong, Z., & Man, H. (2020, September).
 819 Force and Energy Balance of the Dipolarization Front. *Journal of Geophysical*
 820 *Research (Space Physics)*, *125*(9), e28278. doi: 10.1029/2020JA028278
- 821 Sonnerup, B. U. Ö., & Scheible, M. (1998, January). Minimum and Maximum Vari-
 822 ance Analysis. *ISSI Scientific Reports Series*, *1*, 185-220.
- 823 Torbert, R. B., Russell, C. T., Magnes, W., Ergun, R. E., Lindqvist, P.-A., LeCon-
 824 tel, O., ... Lappalainen, K. (2016, March). The FIELDS Instrument Suite
 825 on MMS: Scientific Objectives, Measurements, and Data Products. *Space Sci.*
 826 *Rev.*, *199*, 105-135. doi: 10.1007/s11214-014-0109-8
- 827 Wang, L., Huang, C., Cao, X., Du, A., & Ge, Y. S. (2020, October). Magnetic
 828 Energy Conversion and Transport in the Terrestrial Magnetotail Due to Dipolar-
 829 ization Fronts. *Journal of Geophysical Research (Space Physics)*, *125*(10),
 830 e28568. doi: 10.1029/2020JA028568
- 831 Wolf, R. A., Wan, Y., Xing, X., Zhang, J. C., & Sazykin, S. (2009, September).
 832 Entropy and plasma sheet transport. *Journal of Geophysical Research (Space*
 833 *Physics)*, *114*(A9), A00D05. doi: 10.1029/2009JA014044
- 834 Yang, J., Cao, J. B., Fu, H. S., Wang, T. Y., Liu, W. L., & Yao, Z. H. (2017,
 835 April). Broadband high-frequency waves detected at dipolarization fronts.
 836 *Journal of Geophysical Research (Space Physics)*, *122*(4), 4299-4307. doi:
 837 10.1002/2016JA023465
- 838 Yang, Y., Matthaeus, W. H., Parashar, T. N., Haggerty, C. C., Roytershteyn, V.,
 839 Daughton, W., ... Chen, S. (2017, July). Energy transfer, pressure ten-
 840 sor, and heating of kinetic plasma. *Physics of Plasmas*, *24*(7), 072306. doi:
 841 10.1063/1.4990421
- 842 Yao, Z., Sun, W. J., Fu, S. Y., Pu, Z. Y., Liu, J., Angelopoulos, V., ... Zong, Q. G.
 843 (2013, November). Current structures associated with dipolarization fronts.
 844 *Journal of Geophysical Research (Space Physics)*, *118*(11), 6980-6985. doi:
 845 10.1002/2013JA019290
- 846 Yao, Z. H., Liu, J., Owen, C. J., Forsyth, C., Rae, I. J., Pu, Z. Y., ... Chu, X. N.
 847 (2015, October). A physical explanation for the magnetic decrease ahead
 848 of dipolarization fronts. *Annales Geophysicae*, *33*(10), 1301-1309. doi:
 849 10.5194/angeo-33-1301-2015
- 850 Yao, Z. H., Rae, I. J., Guo, R. L., Fazakerley, A. N., Owen, C. J., Nakamura, R., ...
 851 Zhang, X. J. (2017, April). A direct examination of the dynamics of dipolar-
 852 ization fronts using MMS. *Journal of Geophysical Research (Space Physics)*,
 853 *122*(4), 4335-4347. doi: 10.1002/2016JA023401
- 854 Young, D. T., Burch, J. L., Gomez, R. G., De Los Santos, A., Miller, G. P., Wilson,
 855 P., ... Webster, J. M. (2016, March). Hot Plasma Composition Analyzer for
 856 the Magnetospheric Multiscale Mission. *Space Science Rev.*, *199*, 407-470. doi:
 857 10.1007/s11214-014-0119-6
- 858 Zhong, Z. H., Deng, X. H., Zhou, M., Ma, W. Q., Tang, R. X., Khotyaintsev, Y. V.,
 859 ... Burch, J. L. (2019, November). Energy Conversion and Dissipation at
 860 Dipolarization Fronts: A Statistical Overview. , *46*(22), 12,693-12,701. doi:
 861 10.1029/2019GL085409
- 862 Zhou, M., Huang, S.-Y., Deng, X.-H., & Pang, Y. (2011, October). Observation of a
 863 Sharp Negative Dipolarization Front in the Reconnection Outflow Region. *Chi-*
 864 *nese Physics Letters*, *28*(10), 109402. doi: 10.1088/0256-307X/28/10/109402